Nano Research Energy

ISSN 2791-0091 (print); 2790-8119 (online)
https://doi.org/10.26599/NRE.2024.9120151

Research Article

Bimetallic phosphides-oxides heterostructures coupled heteroatom-doped carbon as bifunctional electrocatalysts for Zn-air batteries

Ruiyu Qi[1,§], Yiliang Shi[1,§], Wenhao Tang[1], Tianli Liu[1], Li Gao[2] (✉), Kewei Teng[1], and Ruiping Liu[1] (✉)

[1] *School of Chemical & Environmental Engineering, China University of Mining & Technology (Beijing), Beijing 100083, China*
[2] *School of Mechanical Engineering, Qinghai University, Xining 810016, China*
[§] *Ruiyu Qi and Yiliang Shi contributed equally to this work.*

Received: 11 October 2024 / **Revised:** 9 December 2024 / **Accepted:** 17 December 2024 / **Published date:** 6 January 2025

ABSTRACT

Designing efficient bifunctional catalysts with multi-component composites is essential for the application of zinc-air batteries (ZABs). Herein, a bimetallic phosphides-oxides heterostructures coupled heteroatom-doped carbon (FeCoP-$FeCo_2O_4$@PNPC) was designed by *in-situ* growth of phosphor-oxide heterostructures on heteroatom-doped carbon materials and employed as bifunctional electrocatalyst for ZABs. The heteroatom-doped carbon substrate with ORR active sites can effectively improve the conductivity and the double transition metal atoms can enhance the catalytic activity. The heterostructure adjusts the d-band center, making the material gain and loss of electrons are at a medium level, which is conducive to the material's capture of raw materials and the release of products. is beneficial to electron transfer. The dense $FeCo_2O_4$ nanorods act as a protection layer to improve stability, and the oxide-phosphide heterostructure and synergistic coupling with the heteroatom-doped carbon substrate also contribute to the catalytic activity. The small ΔE of 0.765 V for catalyzing both OER and ORR, high power density of 121.6 mW·cm^{-2} and the extraordinary long-term stability of more than 240 h for liquid state rechargeable ZAB can be realized. The flexible solid-state rechargeable ZAB with FeCoP-$FeCo_2O_4$@PNPC also exhibits superior mechanical flexibility and cycling stability.

KEYWORDS

bimetallic heterostructures, bifunctional electrocatalyst, heteroatom-doped carbon, zinc-air batteries

1 Introduction

Traditional Li-ion batteries with safety hazards due to Li dendrites, and low specific energy densities (200–250 Wh·kg^{-1}) limit their further application in the electric vehicles, hybrid electric vehicles, grid energy storage and portable devices [1]. Compared with Li-ion battery, metal-air battery with larger specific capacity and energy density have attracted extensive attention as promising clean energy storage system. Among them, zinc-air batteries show great potential due to their low cost, better safety, and high specific energy density (1370 Wh·kg^{-1}, excluded oxygen) [2, 3]. However, the slow reactions occurring at the cathode, namely the oxygen reduction reaction (ORR) during discharge and the oxygen evolution reaction (OER) during charge, and the resulting high overpotential and poor cycling stability hinder the commercial application of zinc-air batteries. An effective approach to break through the bottleneck is to use highly active catalysts [4]. Currently, noble catalysts such as Pt/C for ORR and Ru-based or IrO_2 for OER have been employed to address the sluggish kinetic reactions on Zn-air battery cathodes. However, the scarcity of resources and poor stability limit their further application in Zn-air batteries (ZABs) [5]. Therefore, it is highly desirable to explore noble-metal-free and efficient bifunctional catalysts for Zn-air batteries [6, 7].

Recently, spinel oxides like $MnCo_2O_4$, $ZnCo_2O_4$, $NiCo_2O_4$, $FeCo_2O_4$ have been widely reported as excellent oxygen electrocatalysts owing to synergy effect between the two metal cations in the oxygen catalytic reaction [8–10]. Among them, $FeCo_2O_4$ has been demonstrated as a promising oxygen electrocatalyst due to its redox stability [11, 12]. The catalytic activity of $FeCo_2O_4$ is attributed to the high ratio of Co^{3+}/Co^{2+}, by which oxygen is readily adsorbed to the active sites and Fe^{2+} in the tetrahedral sites can easily release electrons to oxidize to Fe^{3+} at the same time to provide electrons for ORR [13, 14]. However, the poor OER activity of $FeCo_2O_4$ needs to be further improved [15, 16]. Transition metal phosphides (TMPs) have good catalytic activity for OER [17–20], and due to the synergistic effect of two different metals, bimetal phosphides have been reported to improve OER performance more effectively than single metal phosphides [21–23]. However, the poor stability in an oxygen-enriched environment and the unsatisfactory ORR activity of TMPs limit their practical application. In addition, carbon materials doping with two heteroatoms have been shown to be a more effective strategy for improving ORR activity compared to

Address correspondence to Li Gao, 2007990030@qhu.edu.cn; Ruiping Liu, lrp@cumtb.edu.cn

single nitrogen doping [24, 25]. In particular, the ultra-high ORR performance of N, P co-doped carbon catalysts can be attributed to the unique electronic regulation of phosphorus and nitrogen elements [26]. Thus, a visible and effective strategy for the preparation of low-cost bifunctional catalysts is to construct heterogeneously structured transition metal-based catalysts compounded with heteroatom-doped carbon materials [27–31].

Herein, we prepared N, P co-doped porous carbon with phosphorus particles on the surface (cited as PNPC) by one-step pyrolysis of precursors, which was employed as a porous support for nanostructure growth [32]. The iron-doped cobalt phosphide nanoparticles (cited as FeCoP) were *in-situ* synthesized on the surface of the PNPC, followed by further growth of $FeCo_2O_4$ nanorods, and finally forming a phosphide/spinel-type oxide heterostructure on the carbon matrix. After the formation of the heterojunction, the electron gain ability of FeCoP and the electron loss ability of FeCo2O4 will interact with each other, and finally make the heterojunction neither difficult to lose electrons nor difficult to gain electrons, so that it can also play the role of catalytic oxygen reduction of oxygen precipitation reaction. The synthesized FeCoP-$FeCo_2O_4$@PNPC has a large specific surface area and porosity, which provides channels and adsorption sites for intermediates of ORR and OER reactions. The $FeCo_2O_4$ *in-situ* grown on the surface of FeCoP clusters can be regarded as a "protective film", which can improve its stability. Meanwhile, the dense $FeCo_2O_4$ nanorods provide a large specific surface area and pore channels, which will facilitate the rapid transport of oxygen intermediates and improve the stability of OER without affecting its catalytic activity. The synergistic interaction between the bimetallic atoms and the heterojunction interface can optimize the adsorption of oxygen intermediates and improve the bifunctional electrocatalytic activity of FeCoP-$FeCo_2O_4$@PNPC. This work provides a new idea for the design of oxygen electrocatalysts with multi-component coupling structure for application in ZABs.

2 Experimental

2.1 Chemicals and reagents

All the reagents were analytically pure and used without any further treatment. Anhydrous ethanol (C_2H_5OH), dicyandiamide ($C_2H_4N_4$), iron(III) chloride hexahydrate ($FeCl_3·6H_2O$), cobalt(II) chloride hexahydrate, ammonium fluoride (NH_4F), urea (CH_4N_2O), zinc acetate dihydrate ($Zn(Ac)_2$), acrylamide (AM), ammonium persulfate (APS), N, N'-methylenebis (acrylamide) (MBA), potassium hydroxide (KOH), carbon (VXC-72), Nafion solution (5 wt.% in alcohol and water) and zinc foil (thickness of 0.25 mm), and the deionized water.

2.2 Synthesis of PNPC

PNPC were obtained by one-step pyrolysis. Typically, 5 g dicyandiamide was added to 40 mL of DI and stirred at 85 °C for 30 min until complete dissolution. 1.3 mL of phytic acid solution was added slowly to the above solution and stirred at 85 °C for 30 min. The mixed solution was dried in an oven for 36 h to obtain the precursor. The obtained precursor was annealed in Ar at 850 °C for 3 h with a heating rate of 5 °C·min^{-1}, and the resulting product was recorded as PNPC.

2.3 Synthesis of FeCoP@PNPC

676 mg of $CoCl_2·6H_2O$, 540 mg of $FeCl_3·6H_2O$ and 100 mg of the precursor of PNPC were dispersed in 15 mL ethanol under the ultrasonic treatment for 30 min and dried at 60 °C. The mixture was then annealed in Ar atmosphere at 850 °C for 3 h at a rate of 5 °C·min^{-1}. The obtained sample was washed several times with anhydrous ethanol and deionized water, and then freeze-dried in vacuum to obtain protonated FeCoP@PNPC.

2.4 Synthesis of FeCoP-$FeCo_2O_4$@PNPC, $FeCo_2O_4$@PNPC

472 mg of $CoCl_2·6H_2O$, 278 mg of $FeSO_4·7H_2O$, 601 mg of urea, 22.2 mg of NH_4F and 50 mg of as-prepared FeCoP@PNPC were dispersed in 30 mL of DI, after ultrasonic treatment for 30 min, the solution was transferred to a Teflon-lined stainless-steel autoclave and heated at 100 °C for 3 h, and finally the precipitates were collected and washed three times with ethanol and DI, which were then dried in vacuum at 60 °C for 12 h. The obtained samples were annealed at 350 °C for 2 h in air with the heating rate of 5 °C·min^{-1}. The obtained products were denoted as FeCoP-$FeCo_2O_4$@PNPC. The synthesis process of $FeCo_2O_4$@PNPC was the same as that of FeCoP-$FeCo_2O_4$@PNPC, except that FeCoP@PNPC was replaced by PNPC.

2.5 Materials characterization

X-ray diffraction measurements (XRD, Rigaku Ultima IV) were performed with Cu Kα radiation (k = 1.5418 Å). The data were recorded from 10° to 80° with an interval of 0.01° and a scan speed of 10 °·min^{-1}. X-ray photoelectron spectra (XPS) were scaled using a Thermo Scientific K-Alpha X-ray photoelectron spectrometer with the Al Kα radiation as the X-ray source to analyze the elemental composition, valence state and bonding of the positive electrode catalysts. The morphology and structure of the materials were investigated by scanning electron microscope (SEM, GeminiSEM 300, Zeiss) and transmission electron microscope (TEM, JOEL-2100F). All materials were sonicated through an ultrasonic cleaner at 100 W for 15 min in the ice bath to form a relatively homogeneous suspension prior to characterization under the electron microscope. Raman spectroscopy (HR Evolution, Horiba Scientific) was used to analyze the degree of order and disorder of the sample and to identify the substance. The nitrogen adsorption/desorption test was conducted on a Micromeritics ASAP 2460 automated gas sorption system, and the specific surface area and pore size distribution were calculated by the Brunauer-Emmett-Teller method (BET, Micromeritics ASAP 2460).

2.6 Rechargeable Zn-air battery assembling

The aqueous rechargeable Zn-air battery was assembled with a polished Zn anode and an air cathode in the mixture electrolyte of 6 M KOH and 0.2 M $Zn(Ac)_2$. The Zn anode was cut from 3 mm zinc foil with the area of 12 cm^2. The air cathode was composed of a gas diffusion layer (GDL), a current collector layer (carbon cloth), and a spray coated catalyst layer. The catalyst layer was prepared by coating ink in current collector layer. The active area is 0.79 cm^{-2} and the mass loading is controlled at 0.83 mg·cm^{-2}. In general, 10 mg of catalyst was dispersed in a mixed solution of ethanol (10 mL) and Nafion solution (500 μL, 0.5 wt.%) under ultrasonication at 100 W for 30 min in the ice bath to obtain a uniform catalyst ink.

All-solid-state rechargeable Zn-air battery was tested with homemade cell. To assemble the battery, alkaline gel electrolyte (AGE) was prepared with a casual procedure. Specifically, 1 g of poly vinyl alcohol (PVA) was dispersed in 10 mL of DI and stirred

at 95 °C for 1 h. Then, 1 mL of 18 M KOH was added into transparent solution and kept stirring at 95 °C for 30 min, and the gel solution was poured onto glass plate and kept at –20 °C for 24 h to form a robust AGE membrane with a thickness of about 3 mm. The AGE was sandwiched between the Zn foil electrode with thickness of 3 mm and the air electrode (carbon cloth, W0S1009). The active area is 2 cm^2 and the mass loading is about at 0.54 $mg \cdot cm^{-2}$. A piece of airtight tape was used on the side of Zn anode, while a piece of breathable tape with an air inlet of 0.8 cm×0.8 cm was used on the side of air cathode to seal the solid-state ZAB.

2.7 Electrochemical measurements

All electrochemical performances were performed using a CHI 760E electrochemical workstation (CH Instruments, China). All electrochemical measurements were performed in a standard three-electrode system. Graphite electrode and mercury oxide (Hg/HgO) were used as counter electrode (CE) and reference electrode (RE), respectively. The RE was calibrated and all reported potentials were referred to reversible hydrogen electrode (RHE). The potential was calculated to a reversible hydrogen electrode (RHE): $E_{RHE} = E_{Hg/HgO} + 0.098\ V + 0.059\ V \times pH$. The *iR*-compensation was not employed in all electrochemical measurements.

The catalyst ink was prepared by ultrasonically dispersing the mixture of 5 mg of catalyst, 700 μL of deionized water, 200 μL of ethanol (99.7%, Adamas), and 100 μL of 5 wt.% Nafion solution (Sigma-Aldrich) firstly, and then sonicating through an ultrasonic cleaner at 100 W for 30 min. About 20 μL of the catalyst suspension was pipetted and spread onto the RDE (0.196 cm^{-2}) and dried in the air at room temperature. The mass loading of catalyst was controlled to be 0.5 $mg \cdot cm^{-2}$.

For ORR experiment, the electrocatalytic activities were evaluated via the RDE voltammograms in 0.1 M KOH (A.R.) at a rotating speed of 1600 rpm and a scan rate of 10 $mV \cdot s^{-1}$. The electron transfer number (n) was calculated by Koutecky-Levich equation:

$$\frac{1}{j} = \frac{1}{j_k} + \frac{1}{j_L} = \frac{1}{j_k} + \frac{1}{B}\omega^{-1/2}$$

$$B = 0.62nF(D_{(O_2)})^{2/3}\nu^{(-1/6)}C_{(O_2)}$$

$$j_k = \frac{j_L \times j}{j_L - j}$$

Where j is the measured current density, j_k and j_L are the kinetic and diffusion-limitting current densities, ω is the angulat velocity in $rad \cdot s^{-1}$, n is the total number of electrons to be transferred, F is the Faraday constant (96485 $C \cdot mol^{-1}$), D_{O_2} is the diffusion coefficient of oxygen (1.9×10^{-5} $cm^2 \cdot s^{-1}$), ν is the kinetic viscosity of the electrolyte (0.01 $cm^2 \cdot s^{-1}$), and C_{O_2} is the bulk concentration of oxygen (1.2×10^{-6} $mol \cdot cm^{-3}$).

For OER test, the linear sweep voltammetry (LSV) curves were recorded between 1.0 and 1.8 V at a scan rate of 10 $mV \cdot s^{-1}$ in 0.1 M KOH electrolyte solution.

Discharge/charge polarization curves were taken on CHI 760E electrochemical workstation (CH Instruments, Shanghai). Cycling tests were probed by recurrent galvanostatic method for 10 min of discharge followed by 10 min of charge at applied current of 5 $mA \cdot cm^{-2}$ on LAND battery test system. The specific capacity ($mAh \cdot g^{-1}$) was calculated according to the consumed zinc during discharge at a constant current density of 5 $mA \cdot cm^{-2}$. All tests were conducted at room temperature. At the same time, the commercialized Pt/C (20 wt.%) and RuO_2 at a mass ratio of 1:1 was evaluated under the same conditions for comparison.

3 Result and discussion

As shown in Fig. 1(a), the preparation process of FeCoP-$FeCo_2O_4$@PNPC can be divided into three steps. First, the phytic acid was added dropwise into an aqueous solution containing dicyandiamide. After drying the aforementioned solution, carbonize the precipitated solid in an argon atmosphere to obtain porous and layered stacked PNPC. Then the Fe^{3+} and Co^{2+} were introduced into the PNPC by dispersing PNPC and $FeCl_3 \cdot 6H_2O$ and $CoCl_2 \cdot 6H_2O$ in ethanol. Next, the phosphorization process was achieved by sintering the precipitate obtained from drying the aftermentioned solution to produce FeCoP@PNPC which the FeCoP nanoparticle was distributing on the surface of PNPC. Subsequently, the Fe^{3+} and Co^{2+} were introduced into the system again to participate with FeCoP@PNPC in the hydrothermal reaction process. Finally, after sintering the product of hydrothermal reaction, the FeCoP-$FeCo_2O_4$@PNPC covered with *in-situ* growing needle-like $FeCo_2O_4$ which form the heterojunction interface with FeCoP was obtained.

The scanning electron microscopy (SEM) and high-resolution transmission electron microscopy (TEM) was applied to explore the surface morphology and the structure. As shown in Fig. 1(b), the surface of the FeCoP-$FeCo_2O_4$@PNPC exhibits a morphology of nanorod with the length of about 300 nm, which is corresponding to the structure of $FeCo_2O_4$. According to the image of the transmission electron microscope (TEM), the FeCoP-$FeCo_2O_4$@PNPC exhibits a structure of rod shell with and porous lamellar core which is corresponding to the inner porous carbon base (Fig. S1 in the Electronic Supplementary Material (ESM)) and the outer $FeCo_2O_4$ nanorod respectively. In additional, the TEM image (Fig. 1(c)) reveals that there are lots of nanoparticles with the diameter of about 100 nm in the FeCoP-$FeCo_2O_4$@PNPC which is corresponding to the FeCoP dispersed on the surface of the PNPC, which is consistent with Fig. S2 in the ESM. The high-resolution transmission electron microscopy (HRTEM) image (Fig. 1(d)) of Fig. 1(c) shows the heterogeneous interface of three phase. The crystal planes with spacing of 0.243, 0.340, and 0.189 nm correspond to (311) plane of $FeCo_2O_4$, (002) plane of graphite and (211) plane of FeCoP, respectively. The simultaneous existence of the three crystal types suggests the formation of heterojunction. The high-angle annular dark-field scanning transmission electron microscope (HAADF-STEM) and the corresponding energy-dispersive X-ray spectroscopy (EDS) images demonstrate that C, N, O, P, Fe and Co are evenly distributed in the FeCoP-$FeCo_2O_4$@PNPC (Fig. 1(e)). Selected area electron diffraction (SAED) in Fig. 1(f) shows a circular diffraction pattern and is consistent with the main planes of FeCoP, $FeCo_2O_4$ and graphite, revealing the existence of multiple crystal types, which indicating the formation of heterojunction. Figure S3 in the ESM exhibits the XRD patterns of PNPC which has typical peaks locate at 25° and 44°, indexed to (002) plane and (010) plane of graphite, respectively. The diffraction peaks of FeCoP@PNPC are consistent with the orthorhombic CoP (PDF #29-0497) and the orthorhombic FeP (PDF #71-2262). Among the above peaks, the peaks located at 31.6° and 56.8° can be indexed to (011) and (301) planes of CoP, and the peak located at 35.5° can be ascribed to the (120) plane of FeP. Apart from the

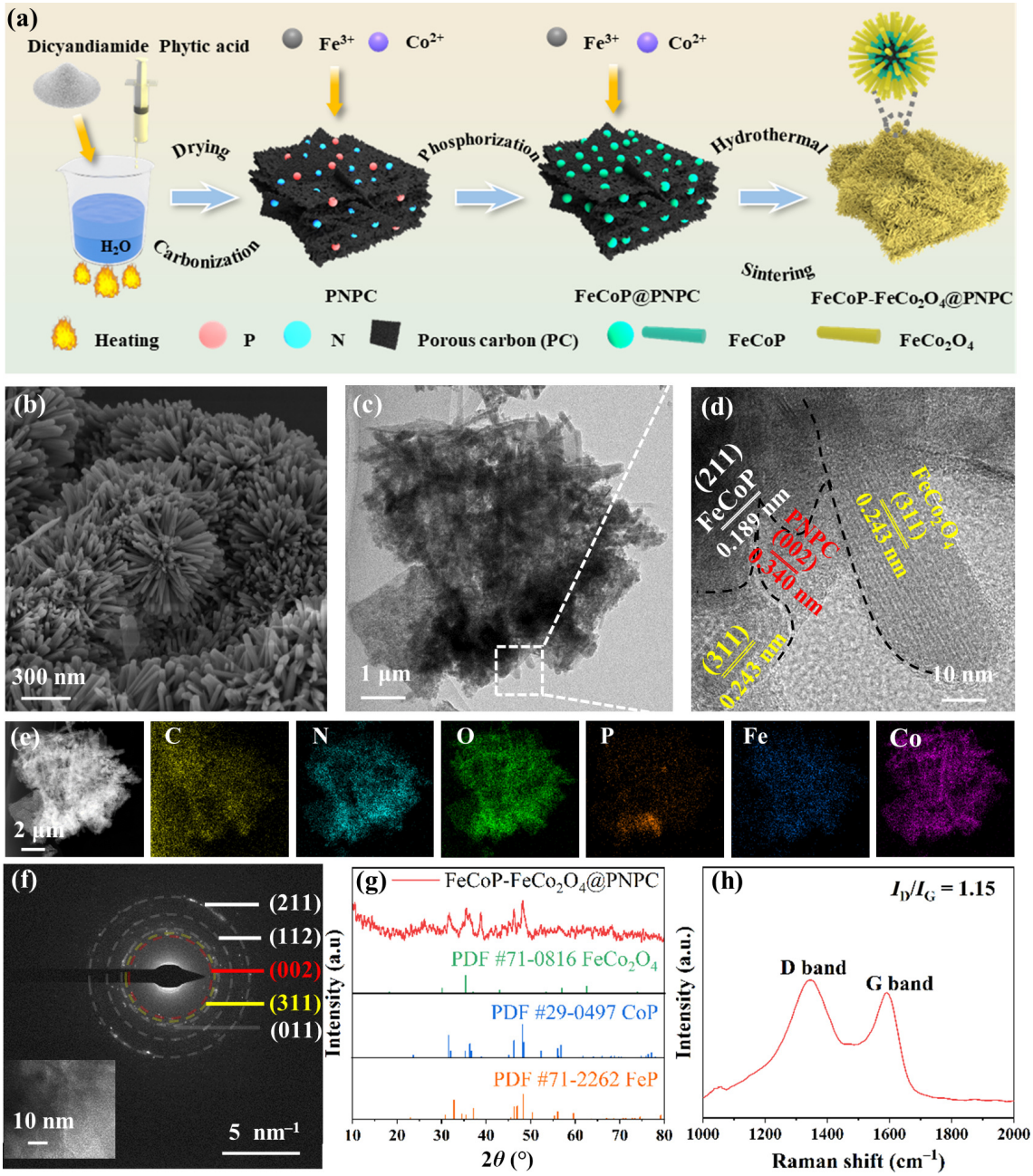

Figure 1 (a) Schematic illustration of the preparation of FeCoP-$FeCo_2O_4$@PNPC. The SEM (b), TEM (c), high resolution TEM (d) and corresponding elemental mapping (e) images of FeCoP-$FeCo_2O_4$@PNPC. (f) HAADF-STEM image of FeCoP-$FeCo_2O_4$@PNPC and the corresponding elemental mapping images. (g) and (h) The XRD pattern and the Raman spectrum of FeCoP-$FeCo_2O_4$@PNPC.

aforementioned, the peak at 36.7° belongs to the superposition of (102) plane in CoP and (111) plane of FeP, the peak at 46.2° indicates the superposition of (112) plane in CoP and (121) plane in FeP, and the peak located at 48.2° indicates the superposition of (211) plane in both CoP and FeP. The above result indicates the successful synthesis of FeCoP. $FeCo_2O_4$@PNPC exhibits four typical peaks at 35.4°, 43.1°, 56.9° and 62.6°, which corresponds to (311), (400), (511) and (440) planes of cubic $FeCo_2O_4$. All the diffraction peaks of FeCoP-$FeCo_2O_4$@PNPC are consistent with the standard FeCoP and $FeCo_2O_4$, indicating the successful construction of the preparation of the FeCoP and $FeCo_2O_4$ and the successful formation of heterogeneous between them (Fig. 1(g)). The Raman spectroscopy was performed to explore the structural characteristics of the as-prepared FeCoP-$FeCo_2O_4$@PNPC, PNPC, FeCoP@PNPC and $FeCo_2O_4$@PNPC. As illustrated in Fig. 1(h), on the surface of the FeCoP-$FeCo_2O_4$@PNPC, there are two obvious peaks at about 1350 and 1580 cm^{-1}, assigning to disordered carbon (D band), which is beneficial for exposing active sites and sp^2-hybridized graphitic carbon (G band) which can enhance the conductivity of the catalyst, respectively [33, 34]. The ratio of the intensity of the D band and G band (I_D/I_G) is an important indicator of the defects degree of material that we generally want to be as high as possible. The I_D/I_G values of FeCoP-$FeCo_2O_4$@PNPC is 1.15, larger than that of PNPC (1.10), FeCoP@PNPC (0.96) and $FeCo_2O_4$@PNPC (1.02) (Fig. S4 in the ESM), which indicate the beneficial structure to enhance the catalytic activity [4]. The N_2 adsorption-desorption isotherm of PNPC and FeCoP-$FeCo_2O_4$@PNPC show a well-defined type-IV hysteresis loop at higher pressure (P/P_0 = 0.6–1.0), indicating the existence of both micropores and mesopores in

PNPC and FeCoP-$FeCo_2O_4$@PNPC (Fig. S5 in the ESM). The main pore size in PNPC is about 2 nm, which indicate there are large number of micropores in PNPC. While the main size of 10 nm can be detected for pores in FeCoP-$FeCo_2O_4$@PNPC, which belongs to the mesopores (Fig. S6 in the ESM).

X-ray photoelectron spectroscopy (XPS) was used to analyze the chemical composition and the valence states of FeCoP@PNPC, $FeCo_2O_4$@PNPC and FeCoP-$FeCo_2O_4$@PNPC. The full spectrums of XPS show the existence of Co, Fe, N, P, O and C in FeCoP@PNPC, $FeCo_2O_4$@PNPC and FeCoP-$FeCo_2O_4$@PNPC (Fig. S7 in the ESM). The presence of phosphorus in the full spectrum of $FeCo_2O_4$@PNPC indicates that phosphorus is successfully doped in the carbon material of PNPC. Figure 2(a) shows the deconvoluted Fe 2p spectra. All the samples show peaks located at about 721.4, 710.4, 724.4 and 711.6 eV, which are assigned to be Fe-N $2p_{1/2}$, Fe-N $2p_{3/2}$, Fe-O $2p_{1/2}$ and Fe-O $2p_{3/2}$, respectively, known as the efficient ORR catalytic sites [35]. Compared to $FeCo_2O_4$@PNPC, the FeCoP@PNPC and FeCoP-$FeCo_2O_4$@PNPC present distinct peaks of Fe-P $2p_{1/2}$ and Fe-P $2p_{3/2}$, which are beneficial for OER process located at about 719.5 and 707.7 eV [36, 37]. Due to the successful growth of $FeCo_2O_4$ shell outside of the FeCoP@PNPC and heterojunction linking between the FeCoP and $FeCo_2O_4$, the position of Fe-P, Fe-N and Fe-O peaks in FeCoP-$FeCo_2O_4$@PNPC exhibit a slight shift towards $FeCo_2O_4$@PNPC compared to FeCoP@PNPC, which is consistent with the conclusion of the peak of P-C-O at 533.6 eV. In the high-resolution Co 2p spectrum, the peaks located at about 781.2, 797.0 eV are assigned to Co-N $2p_{3/2}$ and Co-N $2p_{1/2}$ with ORR catalytic activity [38]. The peaks at about 784.8 and 802.5 eV are ascribed to Co-O $2p_{3/2}$ and Co-O $2p_{1/2}$ of $FeCo_2O_4$ or the native oxide, which also exhibit great catalytic activity for ORR [39]. In the FeCoP@PNPC and FeCoP-$FeCo_2O_4$@PNPC, there are additional peaks at about 778.6 and 786.6 eV, which are ascribed to Co-P $2p_{3/2}$ and Co-P $2p_{1/2}$ with great OER catalytic activity [29]. Similarly, the little shift of Co-P, Co-N and Co-O indicates the interaction between FeCoP and $FeCo_2O_4$ to form the heterojunction (Fig. 2(b)) [40]. In the high-resolution spectra of P 2p (Fig. 2(c)), the existence of metal-phosphorus (M-P) bonds (130.4 and 131.3 eV) and P-C (133.3 eV) indicates the successful doping of P in carbon material and the formation of FeCoP, while the P-O (134.8 eV) may result from bonding between $FeCo_2O_4$ and P of the PNPC or native oxide by contacting with the air [41–43]. Compared to the FeCoP@PNPC, the little shift of peak position of M-P bond of FeCoP-$FeCo_2O_4$@PNPC indicates the formation of heterojunction between the FeCoP and $FeCo_2O_4$ and that the growth of the $FeCo_2O_4$ nanorods does not damage the structure of FeCoP nanoparticles. Moreover, since XPS is a surface analysis technique, the decrease in intensity of the M-P peaks in FeCoP-$FeCo_2O_4$@PNPC may be attributed to the presence of an outer layer of $FeCo_2O_4$. As shown in Fig. 2(d), the N 1s spectrum illustrates five peaks, including pyridinic N (398.5 eV), pyrrolic N (399.4 eV), graphitic N (400.8 eV), metal-N (M-N, 397.6 eV) and oxidized N (403.5 eV) [44, 45]. Among them, pyridinic N and graphitic N with excellent electron-accepting characteristics are the efficient catalytic sites of the ORR, and the content of pyridinic-N and graphitic-N dominates the main proportion of N species. Among all samples, FeCoP-$FeCo_2O_4$@PNPC has the largest proportion of pyridinic N and graphitic N, which indicating its better catalytic activity for ORR. The presence of M-N peak in XPS illustrates the bonding between metals (Fe and Co) and N, which are also the efficient catalytic active sites for ORR. The O 1s spectra can be divided into carbon-oxygen bond (P-C-O) at 533.6 eV, surface-oxygen (M-OH/MOOH) at 531.8 eV, and M-O at 529.8 eV (Fig. S8(a) in the ESM) [46]. Among them, the peak of M-OH/OOH which is the OER active site accounts for the major proportion of the O species, implying the great catalytic activity for OER. The existence of M-O indicates the successful synthesis of $FeCo_2O_4$ and the peak of P-C-O at 533.6 eV implies interaction between FeCoP and $FeCo_2O_4$, which demonstrates the successful growth of $FeCo_2O_4$ and the formation of heterojunction. The C 1s XPS peak (Fig. S8(b) in the ESM) can be deconvoluted into three peaks, which are ascribed to the graphite-like sp^2 carbon bond of C=C/C-C (284.8 eV), heteroatom doping of C-N/P (286.3 eV) and C=O (288.6 eV), indicating the successful doping of N and P elements in carbon material of PNPC [47].

To further investigate the coordination structure and chemical state of Fe and Co, the X-ray absorption near edge structure (XANES) and extended X-ray absorption fine structure (EXAFS)

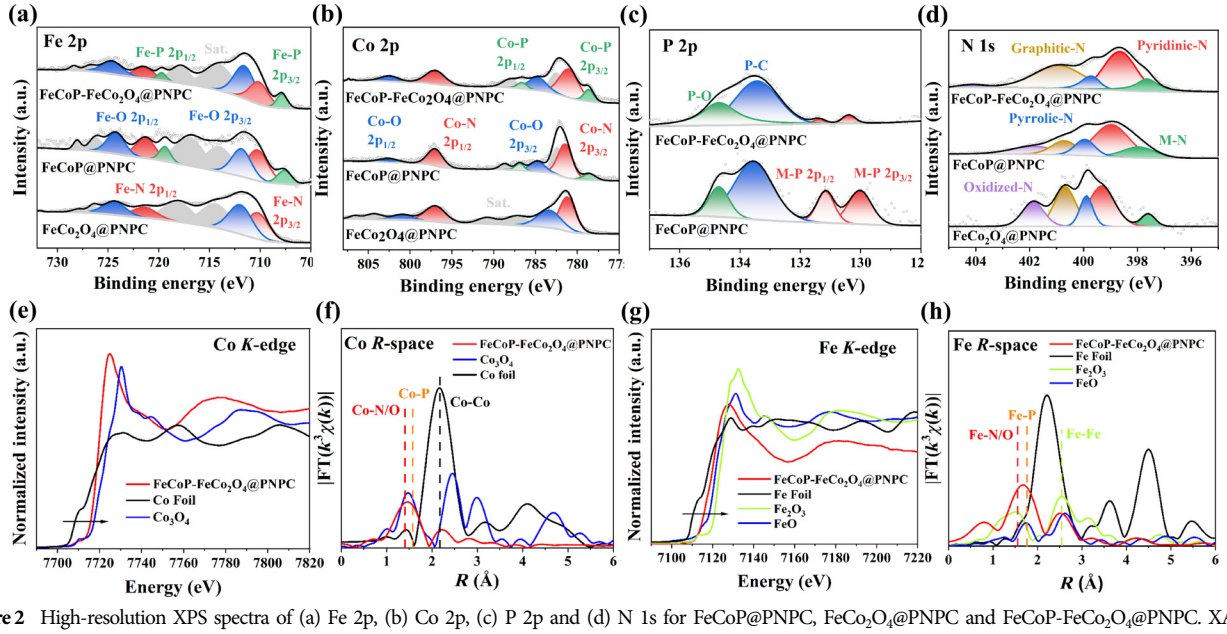

Figure 2 High-resolution XPS spectra of (a) Fe 2p, (b) Co 2p, (c) P 2p and (d) N 1s for FeCoP@PNPC, $FeCo_2O_4$@PNPC and FeCoP-$FeCo_2O_4$@PNPC. XANES spectra at the (e) Co K-edge, (f) FT at Co *R*-space, (g) Fe K-edge and (h) FT at Fe *R*-space.

was investigated. As shown in Fig. 2(e), the Co K-edge absorption threshold position of FeCoP-$FeCo_2O_4$@PNPC locates between those of Co foil and Co_3O_4, indicating the valence state of Co follows the order of Co (Co_3O_4) > Co (FeCoP-$FeCo_2O_4$@PNPC) > Co (Co foil), that is, the valence state of Co in FeCoP-$FeCo_2O_4$@PNPC is between 0 and +3. Based on the energy position of absorption edge and the corresponding oxidation states of standard samples in XANES, the valence of Co in FeCoP-$FeCo_2O_4$@PNPC can be estimated to be 2.16 (Fig. S9(a) in the ESM). It is worth mentioning that the valence state information obtained from XANES is an average result, which imply the valence state of Co in FeCoP-$FeCo_2O_4$@PNPC is caused by the mixing of Co-N/O, Co-P, Co-Co. Similarly, the Fe K-edge absorption threshold position of FeCoP-$FeCo_2O_4$@PNPC locates between those of Fe foil and FeO, indicating the valence state of Fe follows the order of Fe (FeO) > Fe (FeCoP-$FeCo_2O_4$@PNPC) > Fe (Fe foil), that is the valence state of Fe in FeCoP-$FeCo_2O_4$@PNPC is between 0 and +2 (Fig. 2(g)). And the valence state of Fe in FeCoP-$FeCo_2O_4$@PNPC may result from the formation of Fe-O/N, Fe-P and Fe-Fe, which is estimated to be about 1.42 (Fig. S9(b) in the ESM). The coordination information of Co and Fe in FeCoP-$FeCo_2O_4$@PNPC can be confirmed by Fourier-transformed EXAFS (FT-EXAFS) spectra. As shown in Figs. 2(f) and 2(h), compared with the standard reference samples, the peaks of Co(Fe)-N/O, Co(Fe)-P and Co(Fe)-Co(Fe) in Co(Fe) *R*-space can be detected in FeCoP-$FeCo_2O_4$@PNPC at about 1.45(1.52), 1.55(1.75) and 2.18(2.55) Å, which is consistent with the result of XPS analysis [48, 49]. The shell fitting curves and the corresponding EXAFS fitting parameters reveal the detailed coordination information of Co and Fe atoms in FeCoP-$FeCo_2O_4$@PNPC (Fig. S10 and Table S1 in the ESM). *R* factor is an important indicator which represents the degree of difference between the experimental data and the fitted model. In all samples, the values of *R* factor are less than 0.02, which indicates the reliable results of fitting curves. The wavelet transforms (WT) carried out from *R*- and *k*-space with three-dimensional surface mapping provides more intuitive displays of the information of coordination bonds. On one hand, the type of chemical bonds can be determined by theirs values of wave vector in *x*-axis (*k*, Å^{-1}), which is the key factor to distinguish different coordination bonds. On the other hand, the corresponding lengths of coordination bonds can be obtained from the *y*-axis (*R*+Δ*R*, Å). In addition, the *z*-axis of three-dimensional WT can more intuitively exhibits the intensity of different chemical bond vibrations in *k*-space compared to traditional two-dimensional WT spectrum. As shown in Figs. S11(a) and S11(b) in the ESM, compared to the Co foil, the WT of Co in FeCoP-$FeCo_2O_4$@PNPC shows two intensity maximum at about 6 and 8 Å^{-1}, which can be attributed to superposition of Co-N/O (1.4 Å at *R* space) and Co-P (1.7 Å at *R* space) vibrations and Co-Co coordination [50–52]. Similarly, the existence of Fe-N/O (1.5 Å at *R* space), Fe-P (1.8 Å at *R* space) and Fe-Fe in FeCoP-$FeCo_2O_4$@PNPC at about 6 and 8 Å^{-1} can be proved from Figs. S11(c) and S11(d) in the ESM [50, 53, 54]. To ensure that the number of active sites is consistent among the samples, the weight ratio of the active catalyst (FeCoP-$FeCo_2O_4$) and carbon support (PNPC) was set at 55:45 [55], which corresponds to the amount of carbon in the FeCoP-$FeCo_2O_4$@PNPC confirmed through thermogravimetric analysis (TGA) (Fig. S12 in the ESM).

The catalytic activity of ORR performance was tested in an O_2-saturated 0.1 M KOH solution. The cyclic voltammetry (CV) curve of FeCoP-$FeCo_2O_4$@PNPC in a 0.1 M KOH solution saturated with oxygen demonstrates obvious redox peak at about 0.8V, whereas there is no noticeable redox peak in a 0.1 M N_2-saturated KOH solution, indicating the catalytic activity of FeCoP-$FeCo_2O_4$@PNPC for ORR (Fig. S13 in the ESM). The linear sweep voltammetry (LSV) measurements were conducted at 1600 rpm and a scan rate of 10 mV·s^{-1} to evaluate the ORR performances. As shown in Fig. 3(a), FeCoP-$FeCo_2O_4$@PNPC exhibits the highest half-wave potential ($E_{1/2}$) of 0.835 V, which is close to that of the

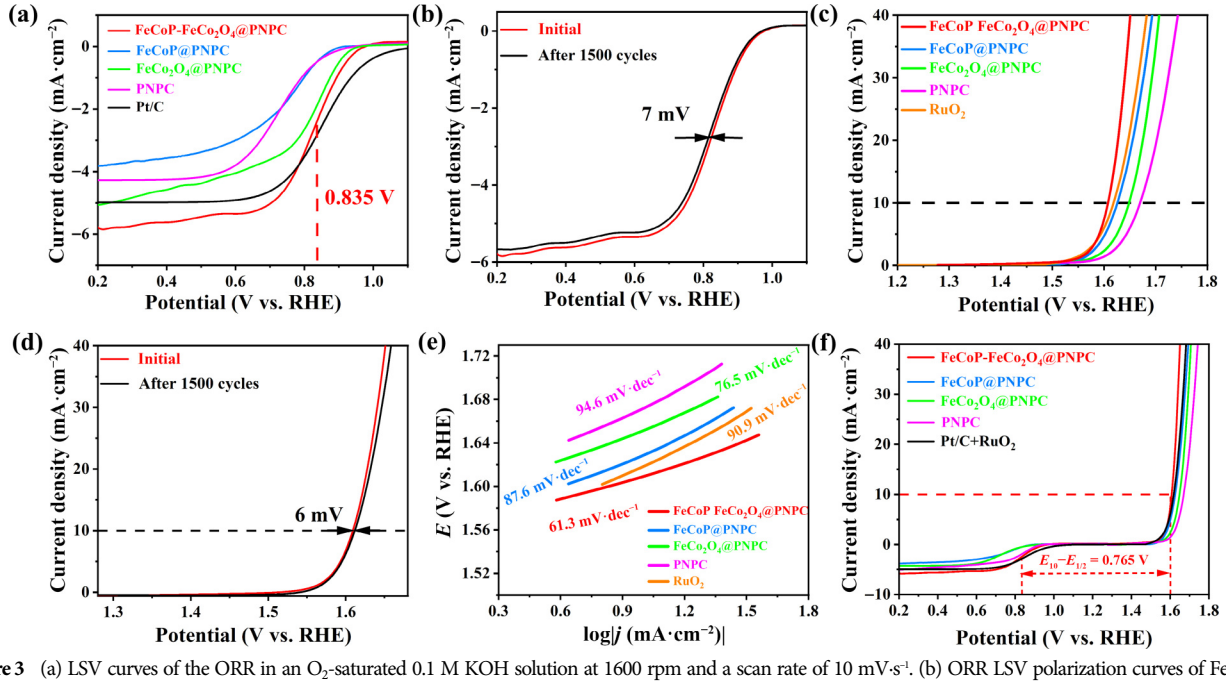

Figure 3 (a) LSV curves of the ORR in an O_2-saturated 0.1 M KOH solution at 1600 rpm and a scan rate of 10 mV·s^{-1}. (b) ORR LSV polarization curves of FeCoP-$FeCo_2O_4$@PNPC for an accelerating stability measurement recorded before and after 1500 cycles. (c) LSV curves of the OER in 0.1 M KOH at 10 mV·s^{-1}. (d) OER LSV polarization curves of FeCoP-$FeCo_2O_4$@PNPC for an accelerating stability measurement recorded before and after 1500 cycles. (e) The OER Tafel plots of PNPC, FeCoP@PNPC, $FeCo_2O_4$@PNPC, FeCoP-$FeCo_2O_4$@PNPC and RuO_2. (f) ORR and OER polarization curves of PNPC, FeCoP@PNPC, $FeCo_2O_4$@PNPC, FeCoP-$FeCo_2O_4$@PNPC and Pt/C+RuO_2.

commercial catalysts (Pt/C+RuO_2, 0.85 V) and is superior to PNPC (0.77 V), FeCoP@PNPC (0.76 V), $FeCo_2O_4$@PNPC (0.83 V) (Fig. S14 in the ESM), revealing the inherent high ORR catalytic activity of $FeCo_2O_4$ and the synergetic effect between the $FeCo_2O_4$ and FeCoP further boost the ORR. In addition, FeCoP-$FeCo_2O_4$@PNPC has the highest current density of 5.9 mA·cm^{-2}, suggesting the high efficiency of FeCoP-$FeCo_2O_4$@PNPC for ORR. To further evaluate the kinetic process of these as-prepared catalysts, the corresponding Tafel plots are displayed in Fig. S15 in the ESM, in which the Tafel slope of FeCoP-$FeCo_2O_4$@PNPC (21.3 mV·dec^{-1}) is lower than other materials indicating faster ORR kinetics. Furthermore, the faster reaction kinetics of the FeCoP-$FeCo_2O_4$@PNPC can be further demonstrated by the EIS spectra in Fig. S16(a) in the ESM. It shows that the FeCoP-$FeCo_2O_4$@PNPC has a lower charge transfer resistance than Pt/C. To explore the catalytic mechanism of ORR, Fig. S17 in the ESM shows the LSV curves at various speeds (400, 600, 900, 1200, 1600 and 2000 rpm). As the rotational speed increases, the limiting current density increases, illustrating the limiting current density is influenced by mass transfer in solution. As shown in the *K-L* plots (Fig. S18 in the ESM) in different potential, the calculated electronic transfer number (n) is 3.9, which demonstrates that FeCoP-$FeCo_2O_4$@PNPC catalyzes the ORR in a four electrons pathway. Moreover, chronoamperometry (Fig. S19 in the ESM) shows that the current density of the FeCoP-$FeCo_2O_4$@PNPC catalyst maintains at 92.7% for 12 h, which is higher than the retention rate observed for Pt/C (86.4%). Cycle experiments were performed to evaluate the catalytic stability of FeCoP-$FeCo_2O_4$@PNPC. After 1500 cycles, the $E_{1/2}$ of FeCoP-$FeCo_2O_4$@PNPC shows a slight shift of only 7 mV and the limiting current density presents a slight decrease, exhibiting the great stability for ORR, which is attributed to the inherent ORR stability of $FeCo_2O_4$ and the protection of heteroatom-doped carbon matrix (Fig. 3(b)).

The catalytic activity of OER was tested in 0.1 M KOH solution. As shown in Fig. 3(c), the LSV curves were tested with three electrode system. Compared to RuO_2 of 386 mV, FeCoP-$FeCo_2O_4$@PNPC shows better OER activity with overpotential (E_{10}) of 370 mV when the current density reached 10 mA·cm^{-2}. Whereas, PNPC, FeCoP@PNPC and $FeCo_2O_4$@PNPC exhibits higher overpotential of 439, 401, and 423 mV respectively (Fig. S20 in the ESM). The result reveals the inherent high OER activity of FeCoP and the synergistic coupling between FeCoP and $FeCo_2O_4$ facilitates the enhancement of OER activity of catalyst. Figure 3(d) exhibits the catalytic stability of OER, after continuous 1500 CV cycles, the overpotential of FeCoP-$FeCo_2O_4$@PNPC increases by only 6 mV, indicating its superior OER stability due to the well protection effect of $FeCo_2O_4$ nanorods grown on the surface of FeCoP. Moreover, a long-term chronopotentiometry test was used to evaluate the OER stability. As shown in Fig. S21 in the ESM, the FeCoP-$FeCo_2O_4$@PNPC catalyst exhibits excellent stability for 12 h, which is better than RuO_2. The Tafel slope is one of the key features for assessing the catalytic kinetics of the catalysts. Figure 3(e) reveals that FeCoP-$FeCo_2O_4$@PNPC exhibits a lower Tafel slop of 61.3 mV·dec^{-1} than that of RuO_2 (90.9 mV·dec^{-1}), PNPC (94.6 mV·dec^{-1}), FeCoP@PNPC (87.6 mV·dec^{-1}) and $FeCo_2O_4$@PNPC (76.5 mV·dec^{-1}), indicating that FeCoP-$FeCo_2O_4$@PNPC is beneficial for accelerating OER kinetics. As shown in Fig. S16(b) in the ESM, the faster OER kinetics of the FeCoP-$FeCo_2O_4$@PNPC can be further demonstrated by its lower charger transfer resistance than RuO_2. To gain a general understanding of the intrinsic activity of as-activated FeCoP-$FeCo_2O_4$@PNPC, turnover frequency (TOF) and electrochemical surface area (ECSA) normalized current density have been estimated. The TOF of FeCoP-$FeCo_2O_4$@PNPC is 1.11 s^{-1} at 1.53 V vs. RHE, which is higher than those of FeCoP@PNPC (0.62 s^{-1}), $FeCo_2O_4$@PNPC (0.46 s^{-1}), PNPC (0.07 s^{-1}) and RuO_2 (0.13 s^{-1}). The ECSA value was measured through the electrochemical double-layer capacitances (C_{dl}) determined by cyclic voltammetry method (Fig. S22 in the ESM). FeCoP-$FeCo_2O_4$@PNPC possesses the C_{dl} value of 12.5 mF·cm^{-2}, which is higher than RuO_2 (7.4 mF·cm^{-2}), indicating that more exposed catalytic active sites are attained by the rod shell structure (Fig. S23 in the ESM). Meanwhile, the ECSA-normalized LSV curves show that the FeCoP-$FeCo_2O_4$@PNPC catalyst exhibits higher current density compared to RuO_2, suggesting its more excellent intrinsic OER catalytic activity (Fig. S24 in the ESM).

The FeCoP-$FeCo_2O_4$@PNPC catalyst collected after the ORR and OER stability tests were characterized to evaluate its stability. After OER/ORR durability test, the HRTEM images (Fig. S25 in the ESM) also showed the presence of two phases, which indicates the unchanged morphology of the FeCoP-$FeCo_2O_4$@PNPC. Moreover, after OER/ORR durability test, the catalyst remained almost unchanged compared to the pristine FeCoP-$FeCo_2O_4$ @PNPC catalyst, which was confirm by the identical diffraction peaks observed in the XRD patterns (Fig. S26 in the ESM) and the Fe, Co, P and N peaks with slightly changed binding energies observed in XPS spectra (Fig. S27 in the ESM). The slight variation in binding energy observed in the XPS results can be attributed to the strong redox reactions occurring during the OER and ORR, as well as the massive P leaching [56]. The high stability of the FeCoP-$FeCo_2O_4$@PNPC observed during the ORR and OER can be attributed to the protection of heteroatom-doped carbon matrix and the well protection effect of $FeCo_2O_4$ nanorods grown on the surface.

The difference between E_{10} of the OER and $E_{1/2}$ of the ORR (i.e., ΔE) is used to evaluate the bifunctionality of the catalyst, and a smaller ΔE typically represents better performance. As shown in Fig. 3(f) and Fig. S28 in the ESM, the ΔE of FeCoP-$FeCo_2O_4$@PNPC is 0.765 V, which is slightly lower than that of the commercial Pt/C and RuO_2 (0.766 V), and superior to PNPC (0.899 V), FeCoP@PNPC (0.871 V) and $FeCo_2O_4$@PNPC (0.823 V), demonstrating its excellent bifunctional catalytic activity. Meanwhile, the bifunctionality of FeCoP-$FeCo_2O_4$@ PNPC also shows some superiority in comparison with other literature (Table S3 in the ESM). From the radar chart of Fig. S29 in the ESM, it is evident that catalyst FeCoP-$FeCo_2O_4$@PNPC demonstrates outstanding performance across all five key indicators of bifunctional oxygen electrocatalysts.

As shown in Fig. 4, the FeCoP-$FeCo_2O_4$@PNPC is composed of PNPC, FeCoP nanoparticle and $FeCo_2O_4$ nanorod. FeCoP is bimetallic phosphide, which has intrinsic activity for OER. In OER, the hydroxide radical will lose electron and convert to the oxygen, the specific equation is as follows: $4OH^- - 4e^- \rightarrow O_2 + 2H_2O$. Therefore, the FeCoP possesses relatively great ability to accept electrons from hydroxide radical, which indicate its relatively low Fermi energy level. On the contrary, the $FeCo_2O_4$ possesses spinel structure, which is beneficial to ORR [57]. The ORR equation is as follows: $O_2 + 4e^- + 2H_2O \rightarrow 4OH^-$, which means the $FeCo_2O_4$ is easy to give electrons to O_2. Therefore, the $FeCo_2O_4$ should possess relatively high Fermi energy level. Due to the differing ease of electron gain and loss during catalytic reactions, charge redistribution occurs when the contact is formed between FeCoP and $FeCo_2O_4$. The driving force for this process is

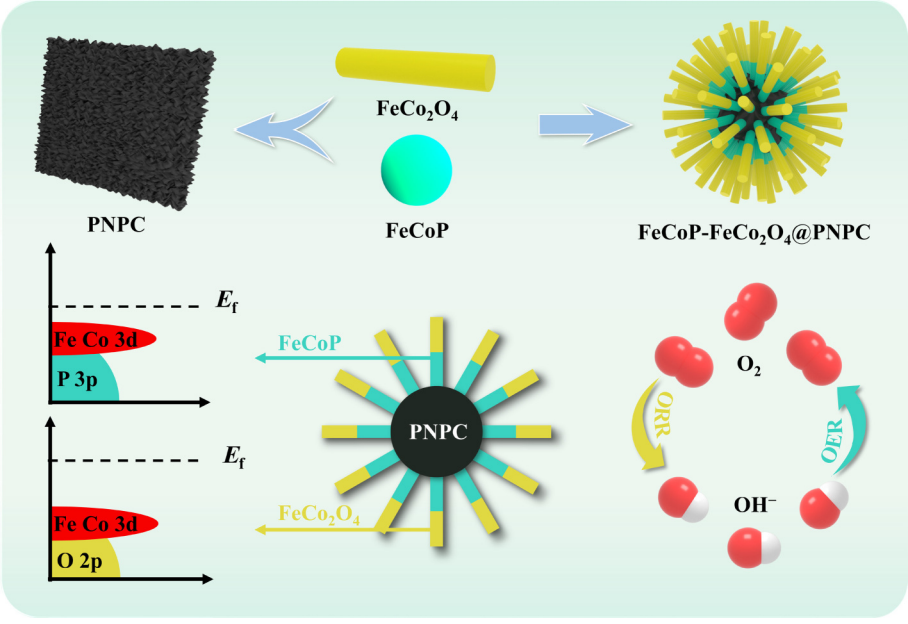

Figure 4 Schematic illustration of the mechanism of bifunctional FeCoP-$FeCo_2O_4$@PNPC.

the work function difference between the two species, which induces a spontaneous transfer of electrons from the material with a lower work function to the one with a higher work function. As a result, upon forming the heterostructure, the contact between the two species leads to the equilibration of their Fermi levels. This phenomenon also gives rise to the formation of an internal electric field [58]. Furthermore, the contact interface exhibits a lower energy barrier, facilitating faster charge transfer and enhancing electrochemical efficiency [59, 60]. In this case, the Fermi energy level of the heterojunction will be at the intermediate level, which will be favorable for the adsorption and desorption of hydroxide or oxygen, and thus exhibits good bifunctional catalytic activity for oxygen precipitation and oxygen reduction.

Owing to the superior catalytic activity and high stability of the FeCoP-$FeCo_2O_4$@PNPC catalyst, herein, we explore the possible practical applicability of FeCoP-$FeCo_2O_4$@PNPC catalyst in aqueous ZAB. As shown in Fig. S30 in the ESM and Fig. 5(a), the aqueous zinc-air battery system is composed of a battery mold made of acrylic, a tank to store which contains 6 M KOH and 0.2 M $Zn(Ac)_2$ electrolyte and a pump to circulate the electrolyte. The FeCoP-$FeCo_2O_4$@PNPC was coated in the air cathode which was composed of a gas diffusion layer (GDL), a current collector layer (carbon paper), and a spray coated catalyst layer. For comparing the performance of aqueous ZABs using different catalysts, an aqueous ZAB with commercial Pt/C and RuO_2 was also assembled in same condition. In Fig. 5(b), the open circuit voltage (OCV)-time curves illustrate that the aqueous ZAB with FeCoP-$FeCo_2O_4$@PNPC deliver the stable OCV of 1.45 V, superior to that of commercial 20 wt.% Pt/C and RuO_2 (1.40 V). The charge/discharge polarization curves (Fig. 5(c)) of aqueous ZAB with FeCoP-$FeCo_2O_4$@PNPC exhibits a smaller charge-discharge voltage difference than that of the ZAB with Pt/C and RuO_2. Meanwhile, the aqueous ZAB with FeCoP-$FeCo_2O_4$@PNPC presents a peak power density of 121.6 mW·cm^{-2} (Fig. 5(d)), which is larger than that of the aqueous ZAB employing Pt/C and RuO_2 as the catalyst (91.9 mW·cm^{-2}). As for the rate performances, the aqueous ZAB with FeCoP-$FeCo_2O_4$@PNPC delivers the voltage of 1.32, 1.29, 1.25, 1.21, and 1.15 V at current density of 1, 2, 5, 10, and 20 mA·cm^{-2}, while the Pt/C and RuO_2 catalyst-based battery outputted the voltage of 1.22, 1.18, 1.09, 0.98, and 0.82 V, respectively (Fig. 5(e)), which shows the outstanding rate performance of aqueous ZAB with FeCoP-$FeCo_2O_4$@PNPC. When the current density reverts back to 1 mA·cm^{-2}, the voltage of ZAB with FeCoP-$FeCo_2O_4$@PNPC still remains at about 1.32 V, indicating the wide voltage adaptation range of aqueous ZAB with FeCoP-$FeCo_2O_4$@PNPC. As shown in Fig. 5(f), the discharge specific capacity of the aqueous ZAB with FeCoP-$FeCo_2O_4$@PNPC is 783.6 mAh·g_{Zn}^{-1} (normalized to the mass of Zn consumed) at 5 mA·cm^{-2}, while the discharge specific capacity of the aqueous ZAB with Pt/C and RuO_2 is 773.7 mAh·g_{Zn}^{-1}. The superb stability can be further manifested by the long-term galvanostatic discharging/charging cycling test. As shown in Fig. 5(g), when cycled at 2 mA·cm^{-2}, the aqueous ZAB with FeCoP-$FeCo_2O_4$@PNPC can be stably cycled for more than 240 h (> 600 cycles), while the aqueous ZAB with Pt/C-RuO_2 can be cycled only for 48 h. Compared with other recently reported bimetallic phosphides and oxides, this work shows a competitive performance (Table S2 in the ESM). In addition, the aqueous ZAB with FeCoP-$FeCo_2O_4$@PNPC exhibits a higher discharging voltage plateau and a lower charging voltage plateau than commercial catalyst, implying the potential of FeCoP-$FeCo_2O_4$@PNPC. In the first few cycles, the ZAB with FeCoP-$FeCo_2O_4$@PNPC exhibits a large round-trip efficiency of 62.5%. After continuous operation for more than 200 h, the round-trip efficiency is only reduced to 60.6%, which indicates the ZAB with FeCoP-$FeCo_2O_4$@PNPC has great cyclic stability.

To demonstrate the potential application in flexible wearable electronic devices, as shown in Fig. 6(a), a flexible quasi-solid-state rechargeable zinc-air battery (FZAB) was assembled using FeCoP-$FeCo_2O_4$@PNPC coated in carbon cloth (CC) as the air cathode, Zn foil as the anode and the polyvinyl alcohol (PVA), an alkaline gel as the electrolyte (AGE). The ZAB assembled with FeCoP-$FeCo_2O_4$@PNPC delivers an OCV of about 1.391 V, while the OCV of the ZAB assembled with Pt/C-RuO_2 is only 1.377 V (Fig. 6(b)). Lower ionic conductivity of AGE compared to aqueous electrolytes may account for the lower open-circuit voltage of the FZAB. Figure 6(c) demonstrates a smaller charge-discharge voltage difference of FZAB with FeCoP-$FeCo_2O_4$@PNPC than that of FZAB with Pt/C-RuO_2. Notably, the corresponding voltage of the flexible FZAB fluctuates at high current densities, which

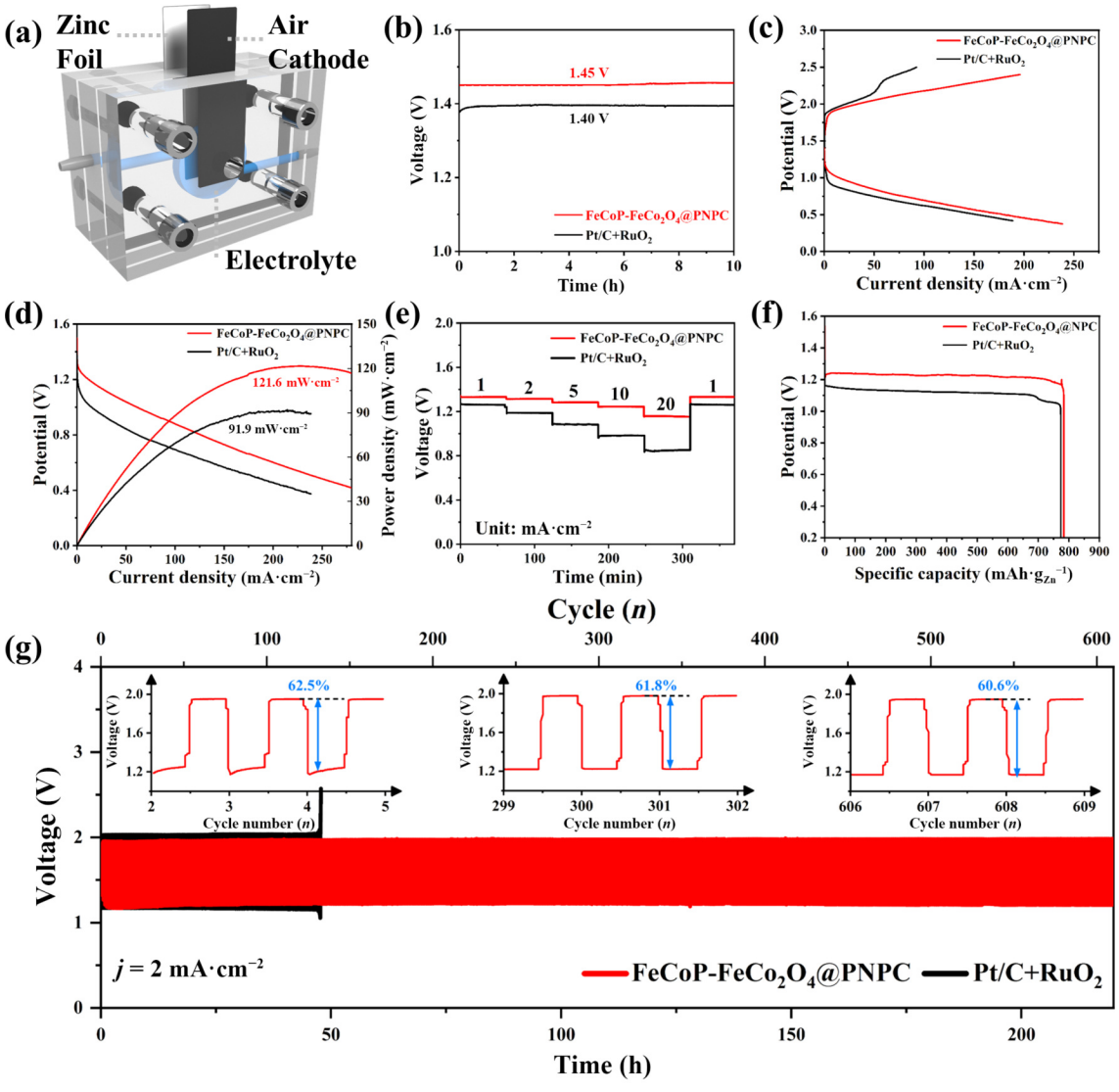

Figure 5 (a) Schematic illustration of the aqueous ZAB. (b) Open-circuit voltages of liquid-state ZABs with FeCoP-$FeCo_2O_4$@PNPC and Pt/C+RuO_2 cathodes. (c) Charge/discharge polarization curves of liquid-state ZABs with FeCoP-$FeCo_2O_4$@PNPC and Pt/C+RuO_2 cathodes. (d) Polarization and power density plots of liquid-state ZABs with FeCoP-$FeCo_2O_4$@PNPC and Pt/C+RuO_2 cathodes. (e) Rate performances of liquid-state ZABs with FeCoP-$FeCo_2O_4$@PNPC and Pt/C+RuO_2 cathodes. (f) Specific capacities at 2 mA·cm^{-2} of liquid-state ZABs with FeCoP-$FeCo_2O_4$@PNPC and Pt/C+RuO_2 cathodes. (g) Cycling stability at 2 mA·cm^{-2} of aqueous ZABs with FeCoP-$FeCo_2O_4$@PNPC and Pt/C+RuO_2 cathodes.

may be due to the change in the state of the AGE as the test time increases. As shown in Fig. 6(d), the FZAB with FeCoP-$FeCo_2O_4$@PNPC exhibits a desirable peak power density of 55.26 mW·cm^{-2}, which is much higher than that of the FZAB with Pt/C-RuO_2 (38.44 mW·cm^{-2}). The FZAB with FeCoP-$FeCo_2O_4$@PNPC also shows good rate performance at sequential current densities (1, 2, 5, 10, 20 and 1 mA·cm^{-2}), exhibiting the more desirable stability and recoverability than that of FZAB employing Pt/C-RuO_2 (Fig. S31 in the ESM). To assess its mechanical flexibility during long-term cycling, the galvanostatic discharging/charging cycling test was conducted at repetitive bending, as depicted in Fig. 6(e). The FZAB with FeCoP-$FeCo_2O_4$@PNPC can be bent to different angles of 0°, 90° and 180°, and stable charge and discharge voltages without obvious decay can be reassured when being bent back to 0°, demonstrating the great flexibility and durability of FeCoP-$FeCo_2O_4$@PNPC. The stability of FZAB was further assessed by galvanostatic cycling at 2 mA·cm^{-2} (Fig. 6(f) in the ESM), and the FZAB with FeCoP-$FeCo_2O_4$@PNPC exhibits stable performance for about 27 h. The undesirable cyclic life is due to the inferior water retention capacity of PVA, which will reduce the conductivity of AGE and cause the increasing polarization of battery voltage.

4 Conclusion

In summary, *in-situ* growth of phosphide-oxide heterojunction on heteroatom-doped carbon materials (FeCoP-$FeCo_2O_4$@PNPC) was successfully prepared and employed as a bifunctional catalyst for ZAB. The FeCoP-$FeCo_2O_4$@PNPC exhibits high porosity and large specific surface area which can provide abundant channels and active sites for catalyzing ORR and OER. $FeCo_2O_4$ *in-situ* grown on the surface of FeCoP can act as a protection layer for the improvement of its electrocatalytic stability. In addition, the synergistic interaction between the bimetallic atoms and the heterojunction interface can adjust the Femi energy level to improve the catalytic activity of FeCoP-$FeCo_2O_4$@PNPC for ORR and OER reactions simultaneously. FeCoP-$FeCo_2O_4$@PNPC exhibits efficient bifunctional performance with a small ΔE of

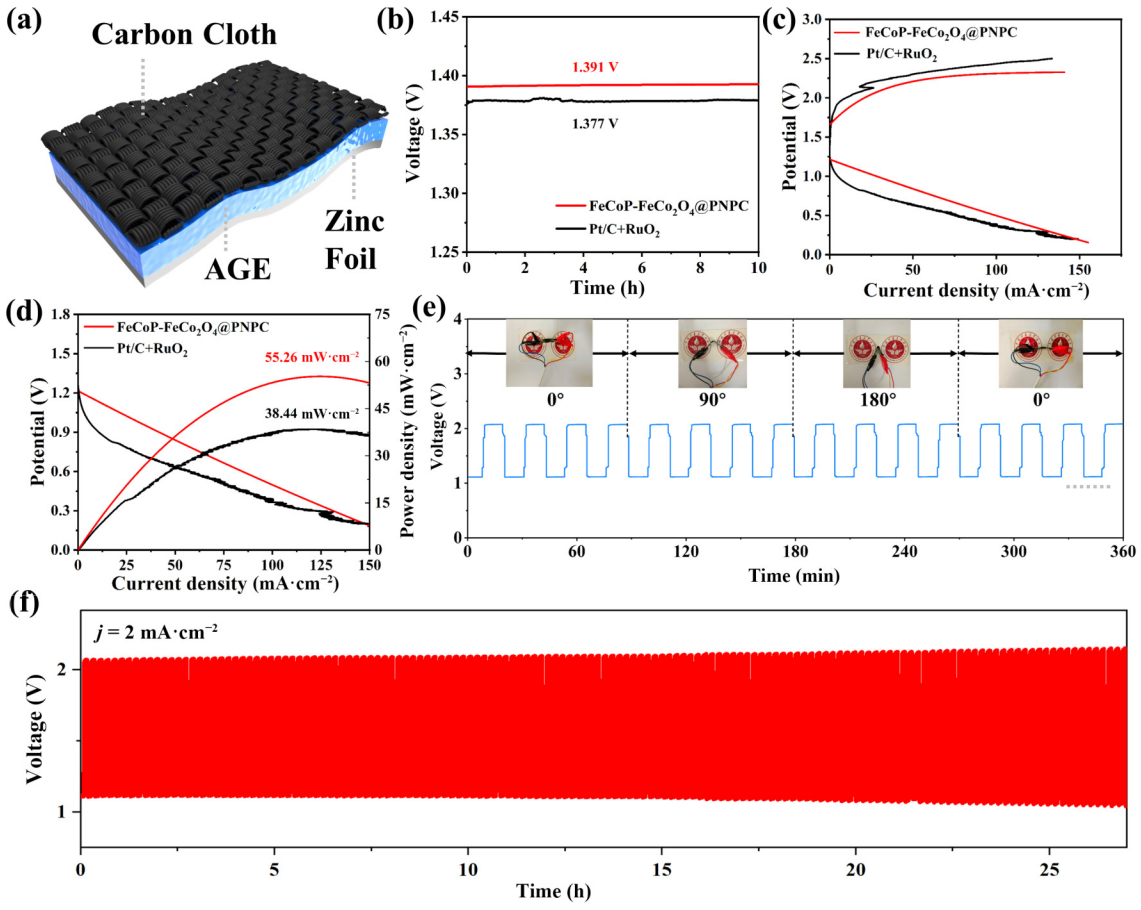

Figure 6 (a) Schematic illustration of a flexible quasi-solid-state ZAB. (b) Open-circuit voltages of the flexible solid-state ZABs with FeCoP-$FeCo_2O_4$@PNPC and Pt/C+RuO_2 cathodes. (c) Charge/discharge polarization curves of flexible solid-state ZABs with FeCoP-$FeCo_2O_4$@PNPC and Pt/C+RuO_2 cathodes. (d) Polarization and power density plots of flexible solid-state ZABs with FeCoP-$FeCo_2O_4$@PNPC and Pt/C+RuO_2 cathodes. (e) Discharging–charging voltage profiles of the ZAB with FeCoP-$FeCo_2O_4$@PNPC at 2 mA·cm^{-2} at the flat and bending conditions in sequence. (f) Cycling stability at 2 mA·cm^{-2} of liquid-state ZABs with FeCoP-$FeCo_2O_4$@PNPC cathodes.

0.765 V for catalyzing both OER and ORR. The battery exhibits the high power density of 121.6 mW·cm^{-2} and the extraordinary long-term stability (more than 240 h) in a aqueous rechargeable ZAB. The flexible solid-state rechargeable ZAB with FeCoP-$FeCo_2O_4$@PNPC also demonstrates superior mechanical flexibility and cycling stability. This work provides a new way for the rational design of a multi-component bifunctional electrocatalyst for zinc-air batteries.

Acknowledgements

This work is supported by the National Natural Science Foundation of China (No. 52272258), the Fundamental Research Funds for the Central Universities (No. 2021JCCXJD01), and Key R&D and transformation projects in Qinghai Province (2023-HZ-801).

Electronic Supplementary Material: Supplementary material (further details of the material, characterizations and electrochemical tests, battery performance etc.) is available in the online version of this article at https://doi.org/10.26599/NRE.2024.9120151.

Declaration of conflicting interests

The authors declare no conflicting interests regarding the content of this article.

Data availability

All data needed to support the conclusions in the paper arepresented in the manuscript and/or the Supplementary Materials. Additional data related to this paper may be requested from the corresponding author upon request.

References

[1] Shen, J.; Zhou, M. M.; Liu, W.; Shi, Y. L.; Tang, W. H.; Deng, Y. R.; Liu, R. P.; Zuo, Y. Z.; Zhang, J. J. Advanced direct recycling technology enables a second life of spent lithium-ion battery. *Energy Storage Mater.*, in press, DOI: 10.1016/j.ensm.2024.103964.

[2] Zhong, X. W.; Shao, Y. F.; Chen, B.; Li, C.; Sheng, J. Z.; Xiao, X.; Xu, B. M.; Li, J.; Cheng, H. M.; Zhou, G. M. Rechargeable zinc-air batteries with an ultralarge discharge capacity per cycle and an ultralong cycle life. *Adv. Mater.* **2023**, *35*, e2301952.

[3] Park, S. H.; Jang, S. Y.; Ahn, S. H. Mass produced flexible aramid electrodes via delamination of layered aerogels for cut-to-fit wearable zinc-air batteries encased in aramid protection. *Energy Environ. Mater.*, in press, DOI: 10.1002/eem2.12804.

[4] Ha, S. J.; Hwang, J.; Kwak, M. J.; Yoon, J. C.; Jang, J. H. Graphene-encapsulated bifunctional catalysts with high activity and durability for Zn-air battery. *Small* **2023**, *19*, e2300551.

[5] Tang, W. H.; Li, B. Y.; Teng, K. W.; Wang, X. D.; Liu, R. P.; Wu, M. W.; Zhang, L.; Ren, P. F.; Zhang, J. Q.; Feng, M. Advanced noble-metal-free bifunctional electrocatalysts for metal-air batteries. *J. Materiomics* **2022**, *8*, 454–474.

[6] Hu, X. L.; Fan, J. C.; Li, X.; Wu, Z. K.; Li, Y. Y.; Xu, C. H. Interfaces engineering of heterostructured NiCoP/NiFe LDH@CC for attaining high catalytic activity in long-lasting rechargeable Zn-air batteries. *Rare Met.* **2024**, *43*, 4961–4972.
[7] Cheng, C.; Zhi, C.; Sun, Z. T.; Ming, Y. Q.; Xiang, T. T.; Zhu, Q. C.; Wu, Z. R.; Li, B.; Li, Y.; Jin, C. et al. Reinforcing oxygen electrocatalytic activity via selective dual-phase heterointerface engineering for rechargeable Zn-air batteries. *Rare Met.* **2024**, *43*, 1524–1536.
[8] Wang, Z. P.; Wu, P. Y.; Zou, X. B.; Wang, S.; Du, L.; Ouyang, T.; Liu, Z. Q. Optimizing the oxygen-catalytic performance of Zn–Mn–Co spinel by regulating the bond competition at octahedral sites. *Adv. Funct. Mater.* **2023**, *33*, 2214275.
[9] Kim, J.; Ko, W.; Yoo, J. M.; Paidi, V. K.; Jang, H. Y.; Shepit, M.; Lee, J.; Chang, H.; Lee, H. S.; Jo, J. et al. Structural insights into multi-metal spinel oxide nanoparticles for boosting oxygen reduction electrocatalysis. *Adv. Mater.* **2022**, *34*, e2107868.
[10] Tan, R. F.; Jeong, Y. J.; Li, Q.; Kang, M.; Cho, I. S. Defect-rich spinel ferrites with improved charge collection properties for efficient solar water splitting. *J. Adv. Ceram.* **2023**, *12*, 612–624.
[11] Patta, P.; Chen, Y. Y.; Natesan, M.; Sung, C. L.; Yang, C. C.; Wang, C. H.; Fujigaya, T.; Chang, Y. H. Investigation of Zn-substituted $FeCo_2O_4$ for the oxygen evolution reaction and reaction mechanism monitoring through *in situ* near-ambient-pressure X-ray photoelectron spectroscopy. *ACS Catal.* **2023**, *13*, 13434–13445.
[12] Sun, Z. H.; Cao, X. C.; Gonzalez Martinez, I. G.; Rümmeli, M. H.; Yang, R. Z. Enhanced electrocatalytic activity of $FeCo_2O_4$ interfacing with CeO_2 for oxygen reduction and evolution reactions. *Electrochem. Commun.* **2018**, *93*, 35–38.
[13] Li, L.; Zhang, Q. C.; He, B.; Pan, R.; Wang, Z. X.; Chen, M. X.; Wang, Z.; Yin, K. B.; Yao, Y. G.; Wei, L. et al. Advanced multifunctional aqueous rechargeable batteries design: From materials and devices to systems. *Adv. Mater.* **2022**, *34*, 2104327–2104336.
[14] Wang, X. T.; Ouyang, T.; Wang, L.; Zhong, J. H.; Ma, T. Y.; Liu, Z. Q. Redox-inert Fe^{3+} ions in octahedral sites of Co–Fe spinel oxides with enhanced oxygen catalytic activity for rechargeable zinc-air batteries. *Angew. Chem., Int. Ed.* **2019**, *58*, 13291–13296.
[15] Lei, Z. H.; Lee, J. M.; Singh, G.; Sathish, C. I.; Chu, X. Z.; Al-Muhtaseb, A. H.; Vinu, A.; Yi, J. B. Recent advances of layered-transition metal oxides for energy-related applications. *Energy Storage Mater.* **2021**, *36*, 514–550.
[16] Hao, S. Y.; Chen, L. C.; Yu, C. L.; Yang, B.; Li, Z. J.; Hou, Y.; Lei, L. C.; Zhang, X. W. NiCoMo hydroxide nanosheet arrays synthesized via chloride corrosion for overall water splitting. *ACS Energy Lett.* **2019**, *4*, 952–959.
[17] Zhao, S. L.; Ran, S. Y.; Shi, N.; Liu, M. L.; Sun, W.; Yu, Y.; Zhu, Z. H. Structural design induced electronic optimization in single-phase MoCoP nanocrystal for boosting oxygen reduction, oxygen evolution, and hydrogen evolution. *Small* **2023**, *19*, e2302414.
[18] Wang, X. B.; Hou, Z. C.; Zhan, N. N.; Guo, Z. J.; Zhao, Y. Electronic-ferry in metal element migration promoting deep activation of NiFe based phosphide for high efficient and stable oxygen evolution reaction. *Appl. Catal. B: Environ.* **2024**, *340*, 123186.
[19] Yang, N. W.; Tian, S. N.; Feng, Y. J.; Hu, Z. Y.; Liu, H.; Tian, X. L.; Xu, L.; Hu, C. Q.; Yang, J. Introducing high-valence iridium single atoms into bimetal phosphides toward high-efficiency oxygen evolution and overall water splitting. *Small* **2023**, *19*, e2207253.
[20] Zeng, X. J.; Zhang, Q. Q.; Jin, C. L.; Huang, H.; Gao, Y. F. Fe-induced electronic transfer and structural evolution of lotus pod-like $CoNiFeP_x$@P, N–C heterostructure for sustainable oxygen evolution. *Energy Environ. Mater.* **2024**, *7*, e12628.
[21] Jiang, J.; Zhou, X. L.; Lv, H. G.; Yu, H. Q.; Yu, Y. Bimetallic-based electrocatalysts for oxygen evolution reaction. *Adv. Funct. Mater.* **2023**, *33*, 2212160.
[22] Gao, L.; Chang, S. M.; Zhang, Z. Y. High-quality CoFeP nanocrystal/N, P dual-doped carbon composite as a novel bifunctional electrocatalyst for rechargeable Zn-air battery. *ACS Appl. Mater. Interfaces* **2021**, *13*, 22282–22291.
[23] Sun, S. F.; Zhou, X.; Cong, B. W.; Hong, W. Z.; Chen, G. Tailoring the d-band centers endows $(Ni_xFe_{1-x})_2P$ nanosheets with efficient oxygen evolution catalysis. *ACS Catal.* **2020**, *10*, 9086–9097.
[24] Wei, L. C.; Zhang, Y. F.; Yang, Y.; Ye, M. H.; Li, C. C. Manipulating the electronic structure of graphite intercalation compounds for boosting the bifunctional oxygen catalytic performance. *Small* **2022**, *18*, e2107667.
[25] Lai, C. L.; Li, M.; Shen, Y.; Zhou, M.; Wang, W.; Jiang, K.; Li, H. M.; Wang, K. L. *In situ* coupling of highly dispersed Ni/Fe metal-NC sites and N-doped 3D carbon fibers toward free-standing bifunctional cathode for flexible zinc-air battery. *Energy Environ. Mater.* **2024**, *7*, e12541.
[26] Rao, P.; Luo, J. M.; Wu, D. X.; Li, J.; Chen, Q.; Deng, P. L.; Shen, Y. J.; Tian, X. L. Isolated Co atoms anchored on defective nitrogen-doped carbon graphene as efficient oxygen reduction reaction electrocatalysts. *Energy Environ. Mater.* **2022**, *6*, e12371.
[27] Yao, Y.; Wu, J. X.; Feng, Q. X.; Zeng, K.; Wan, J.; Zhang, J. C.; Mao, B. Y.; Hu, K.; Chen, L. M.; Zhang, H. et al. Spontaneous internal electric field in heterojunction boosts bifunctional oxygen electrocatalysts for zinc-air batteries: Theory, experiment, and application. *Small* **2023**, *19*, 2302015.
[28] Niu, H. J.; Lin, S. Y.; Chen, Y. P.; Feng, J. J.; Zhang, Q. L.; Wang, A. J. Hydrogel derived FeCo/FeCoP embedded in N, P-codoped 3D porous carbon framework as a highly efficient electrocatalyst for oxygen reduction reaction. *Appl. Surf. Sci.* **2021**, *536*, 147950.
[29] Shi, Q.; Liu, Q.; Zheng, Y. P.; Dong, Y. Q.; Wang, L.; Liu, H. T.; Yang, W. Y. Controllable construction of bifunctional Co_xP@N,P-doped carbon electrocatalysts for rechargeable zinc-air batteries. *Energy Environ. Mater.* **2022**, *5*, 515–523.
[30] Tang, W. H.; Teng, K. W.; Guo, W. G.; Gu, F.; Li, B. Y.; Qi, R. Y.; Liu, R. P.; Lin, Y. Y.; Wu, M. M.; Chen, Y. H. Defect-engineered Co_3O_4@nitrogen-deficient graphitic carbon nitride as an efficient bifunctional electrocatalyst for high-performance metal-air batteries. *Small* **2022**, *18*, 2202194.
[31] Wu, S.; Wu, D.; Zhang, D. W.; Liu, W. H.; Luo, H.; He, J. B.; Yang, Q. C.; Li, Z. W.; Liu, R. P. Boosting the activity and stability with dual-metal-N couplings for Li–O_2 battery. *Energy Environ. Mater.* **2022**, *5*, 918–927.
[32] Guo, K.; Qu, G.; Li, J.; Xia, H. C.; Yan, W. F.; Fu, J. W.; Yuan, P. F.; Zhang, J. N. Polysulfides shuttling remedies by interface-catalytic effect of Mn_3O_4-MnP_x heterostructure. *Energy Storage Mater.* **2021**, *36*, 496–503.
[33] Lyu, Z.; Yu, S.; Wang, M. Y.; Tieu, P.; Zhou, J. C.; Shi, Q. R.; Du, D.; Feng, Z. X.; Pan, X. Q.; Lin, H. F. et al. NiFe nanoparticle nest supported on graphene as electrocatalyst for highly efficient oxygen evolution reaction. *Small* **2024**, *20*, 2308278.
[34] Yang, J.; Zhu, G. X.; Liu, Y. J.; Xia, J. X.; Ji, Z. Y.; Shen, X. P.; Wu, S. K. Fe_3O_4-decorated Co_9S_8 nanoparticles *in situ* grown on reduced graphene oxide: A new and efficient electrocatalyst for oxygen evolution reaction. *Adv. Funct. Mater.* **2016**, *26*, 4712–4721.
[35] Jiang, W. J.; Gu, L.; Li, L.; Zhang, Y.; Zhang, X.; Zhang, L. J.; Wang, J. Q.; Hu, J. S.; Wei, Z. D.; Wan, L. J. Understanding the high activity of Fe–N–C electrocatalysts in oxygen reduction: Fe/Fe_3C nanoparticles boost the activity of Fe–N_x. *J. Am. Chem. Soc.* **2016**, *138*, 3570–3578.
[36] Deng, Y. W.; Cao, Y. F.; Xia, Y.; Xi, X. Y.; Wang, Y.; Jiang, W. F.; Yang, D.; Dong, A. G.; Li, T. T. Self-templated synthesis of CoFeP@C cage-in-cage superlattices for enhanced electrocatalytic water splitting. *Adv. Energy Mater.* **2022**, *12*, 2202394.
[37] Chen, Q. M.; Zhang, Q. C.; Liu, H. B.; Liang, J. M.; Peng, W. C.; Li, Y.; Zhang, F. B.; Fan, X. B. Preparation of hollow cobalt-iron phosphides nanospheres by controllable atom migration for enhanced water oxidation and splitting. *Small* **2021**, *17*, 2007858.
[38] Ding, K. X.; Hu, J. G.; Luo, J.; Zhao, L. M.; Jin, W.; Liu, Y. P.; Wu, Z. H.; Zou, G. Q.; Hou, H. S.; Ji, X. B. Robust electronic correlation of Co–CoN_4 hybrid active sites for durable rechargeable Zn-air batteries. *Adv. Funct. Mater.* **2022**, *32*, 2207331.

[39] Zhao, Y. L.; Wang, X. Y.; Guo, X. M.; Shi, N.; Cheng, D. D.; Zhou, H.; Saito, N.; Fan, T. X. Nitrogen-doped 3D porous graphene coupled with densely distributed CoO_x nanoparticles for efficient multifunctional electrocatalysis and Zn-air battery. *Electrochim. Acta* **2022**, *420*, 140432.
[40] Zhang, W.; Guo, X. M.; Li, C.; Xue, J. Y.; Xu, W. Y.; Niu, Z.; Gu, H. W.; Redshaw, C.; Lang, J. P. Ultralong nitrogen/sulfur Co-doped carbon nano-hollow-sphere chains with encapsulated cobalt nanoparticles for highly efficient oxygen electrocatalysis. *Carbon Energy* **2023**, *5*, e317.
[41] Ma, R.; Cui, X.; Xu, X. X.; Wang, Y. L.; Xiang, G. Q.; Gao, L. K.; Lin, Z. Q.; Yang, Y. K. Collaborative integration of ultrafine Fe_2P nanocrystals into Fe, N, P-codoped carbon nanoshells for highly-efficient oxygen reduction. *Nano Energy* **2023**, *108*, 108179.
[42] Huang, Y. B.; Zhang, M.; Liu, P.; Cheng, F. L.; Wang, L. S. Co_3O_4 supported on N, P-doped carbon as a bifunctional electrocatalyst for oxygen reduction and evolution reactions. *Chin. J. Catal.* **2016**, *37*, 1249–1256.
[43] Maiti, K.; Kim, K.; Noh, K. J.; Han, J. W. Synergistic coupling ensuing cobalt phosphosulfide encapsulated by heteroatom-doped two-dimensional graphene shell as an excellent catalyst for oxygen electroreduction. *Chem. Eng. J.* **2021**, *423*, 130233.
[44] Zhang, X. R.; Wen, X. Y.; Pan, C.; Xiang, X.; Hao, C.; Meng, Q. H.; Tian, Z. Q.; Shen, P. K.; Jiang, S. P. N species tuning strategy in N, S co-doped graphene nanosheets for electrocatalytic activity and selectivity of oxygen redox reactions. *Chem. Eng. J.* **2022**, *431*, 133216.
[45] Liu, Y. Y.; Tu, F. D.; Zhang, Z. Y.; Zhao, Z. G.; Guo, P.; Shen, L. X.; Zhang, Y. L.; Zhao, L.; Shao, G. J.; Wang, Z. B. Molecular scissor tailoring hierarchical architecture of ZIF-derived Fe/N/C catalysts for acidic oxygen reduction reaction. *Appl. Catal. B: Environ.* **2023**, *324*, 122209.
[46] Wu, W.; Chen, R. Z.; Chen, S. H.; Wang, Z. C.; Cheng, N. C. Optimizing d-orbital electronic configuration via metal-metal oxide core-shell charge donation for boosting reversible oxygen electrocatalysis. *Small* **2023**, *19*, 2300621.
[47] Jose, V.; Nsanzimana, J. M. V.; Hu, H. M.; Choi, J.; Wang, X.; Lee, J. M. Highly efficient oxygen reduction reaction activity of N-doped carbon-cobalt boride heterointerfaces. *Adv. Energy Mater.* **2021**, *11*, 2100157.
[48] Chu, P. P.; Zhang, Y. M.; He, J. J.; Chen, J. H.; Zhuang, J. J.; Li, Y. L.; Ren, X. Z.; Zhang, P. X.; Sun, L. N.; Yu, B. Z. et al. Defective Fe_3O_{4-x} few-atom clusters anchored on nitrogen-doped carbon as efficient oxygen reduction electrocatalysts for high-performance zinc-air batteries. *Small Methods* **2022**, *6*, 2200207.
[49] Fan, H. S.; Liang, X. Y.; Ma, F. X.; Zhang, G. B.; Liu, Z. Q.; Zhen, L.; Zeng, X. C.; Xu, C. Y. Low-potential iodide oxidation enables dual-atom CoFe–N–C catalysts for ultra-stable and high-energy-efficiency Zn-air batteries. *Small* **2023**, *20*, e2307863.
[50] Liu, Z. C.; Zhang, T.; Lin, Y.; Jia, H. R.; Wang, Y. Q.; Wang, Y. Y.; Zhang, G. X. Highly N-doped Fe/Co phosphide superstructures for efficient water splitting. *Small* **2023**, *19*, 2302475.
[51] Pei, Z. H.; Zhang, H. B.; Guo, Y.; Luan, D. Y.; Gu, X. J.; Lou, X. W. Atomically dispersed Fe sites regulated by adjacent single Co atoms anchored on N–P Co-doped carbon structures for highly efficient oxygen reduction reaction. *Adv. Mater.* **2024**, *36*, 2306047.
[52] Sa, Y. J.; Seo, D. J.; Woo, J.; Lim, J. T.; Cheon, J. Y.; Yang, S. Y.; Lee, J. M.; Kang, D.; Shin, T. J.; Shin, H. S. et al. A general approach to preferential formation of active Fe–N_x sites in Fe–N/C electrocatalysts for efficient oxygen reduction reaction. *J. Am. Chem. Soc.* **2016**, *138*, 15046–15056.
[53] Liu, H.; Jiang, L. Z.; Sun, Y. Y.; Khan, J.; Feng, B.; Xiao, J. M.; Zhang, H. D.; Xie, H. J.; Li, L. N.; Wang, S. Y. et al. Revisiting the role of sulfur functionality in regulating the electron distribution of single-atomic Fe sites toward enhanced oxygen reduction. *Adv. Funct. Mater.* **2023**, *33*, 2304074.
[54] Fu, C.; Qi, X. Q.; Zhao, L.; Yang, T. T.; Xue, Q.; Zhu, Z. Z.; Xiong, P.; Jiang, J. X.; An, X. G.; Chen, H. Y. et al. Synergistic cooperation between atomically dispersed Zn and Fe on porous nitrogen-doped carbon for boosting oxygen reduction reaction. *Appl. Catal. B: Environ.* **2023**, *335*, 122875.
[55] Li, X. Q.; Cheng, B. J.; Guan, G. G.; Zhang, X. K.; Zhang, K. Y.; Xiang, J. Flexible electrospun FeCo/carbon hybrid nanofiber films as binder-free anodes for enhanced lithium storage performance. *Electrochim. Acta* **2023**, *454*, 142420.
[56] Yang, X. F.; Wang, F. B.; Jing, Z. X.; Chen, M.; Wang, B.; Wang, L.; Qu, G. M.; Kong, Y. Y.; Xu, L. Q. A general "*in situ* etch-adsorption-phosphatization" strategy for the fabrication of metal phosphides/hollow carbon composite for high performance liquid/flexible Zn-air batteries. *Small* **2023**2301985.
[57] Zhong, H. X.; Zhang, Y.; Zhang, X. B. Superior oxygen reduction electrocatalyst: Hollow porous spinel microsphere. *Chem* **2018**, *4*, 196–198.
[58] Yu, C. Y.; Tan, M. X.; Tao, C. D.; Hou, Y. X.; Liu, C. B.; Meng, H. M.; Su, Y. J.; Qiao, L. J.; Bai, Y. Remarkably enhanced piezo-photocatalytic performance in $BaTiO_3$/CuO heterostructures for organic pollutant degradation. *J. Adv. Ceram.* **2022**, *11*, 414–426.
[59] Feng, C.; Lv, M. Y.; Shao, J. X.; Wu, H. Y.; Zhou, W. L.; Qi, S.; Deng, C.; Chai, X. Y.; Yang, H. P.; Hu, Q. et al. Lattice strain engineering of Ni_2P enables efficient catalytic hydrazine oxidation-assisted hydrogen production. *Adv. Mater.* **2023**, *35*, 2305598.
[60] Yang, Y. F.; Li, X. Y.; Liu, G. L.; Liu, H. X.; Shi, Y. H.; Ye, C. M.; Fang, Z.; Ye, M. X.; Shen, J. F. Hierarchical ohmic contact interface engineering for efficient hydrazine-assisted hydrogen evolution reaction. *Adv. Mater.* **2024**, *36*, 2307979.

Ruiyu Qi is currently a graduate student at China University of Mining & Technology (Beijing). His research interests focus on Zinc-air battery.

Yiliang Shi is currently a graduate student at China University of Mining & Technology (Beijing). His research interests focus on zinc-air battery.

Li Gao is an associate professor at the school of mechanical engineering, Qinghai University. Her major research mainly focused on the polymer processing technology and applications in battery and catalysts.

Ruiping Liu received his PhD (2011) in materials science from China University of Mining & Technology (Beijing), then he joined Chang-An Wang's group at Tsinghua University (2012-2013) as a postdoctoral fellow and Zhiqun Lin's group at the Georgia Institute of Technology, USA (2016-2017) as a visiting Scholar. He is currently a full professor at school of chemical & environmental engineering, China University of Mining & Technology (Beijing). His major research mainly focused on the synthesis of functional materials, and their applications in battery and catalysts.